

## MIT Open Access Articles

### *Assessing the Device-performance Impacts of Structural Defects with TCAD Modeling*

The MIT Faculty has made this article openly available. **Please share** how this access benefits you. Your story matters.

**Citation:** Needleman, David Berney et al. "Assessing the Device-Performance Impacts of Structural Defects with TCAD Modeling." *Energy Procedia* 77 (2015): 8–14.

**As Published:** <http://dx.doi.org/10.1016/j.egypro.2015.07.003>

**Publisher:** Elsevier

**Persistent URL:** <http://hdl.handle.net/1721.1/107413>

**Version:** Final published version: final published article, as it appeared in a journal, conference proceedings, or other formally published context

**Terms of use:** Creative Commons Attribution-NonCommercial-NoDerivs License



5th International Conference on Silicon Photovoltaics, SiliconPV 2015

## Assessing the device-performance impacts of structural defects with TCAD modeling

David Berney Needleman<sup>a</sup>, Hannes Wagner<sup>a</sup>, Pietro P. Altermatt<sup>b</sup>, Tonio Buonassisi<sup>a\*</sup>

<sup>a</sup>Massachusetts Institute of Technology, Cambridge, MA, 02139, USA

<sup>b</sup>Leibniz University of Hannover, Dept. Solar Energy, Appelstr. 2, 30167 Hannover, Germany

---

### Abstract

Advanced solar cell architectures like passivated emitter and rear (PERC) and heterojunction with intrinsic thin layer (HIT) are increasingly sensitive to bulk recombination. Present device models consider homogeneous bulk lifetime, which does not accurately reflect the effects of heterogeneously distributed defects. To determine the efficiency potential of multicrystalline silicon (mc-Si) in next-generation architectures, we present a higher-dimensional numerical simulation study of the impacts of structural defects on solar cell performance. We simulate these defects as an interfacial density of traps with a single mid-gap energy level using Shockley-Read-Hall (SRH) statistics. To account for enhanced recombination at the structural defects, we apply a linear scaling to the majority-carrier capture cross-section and scale the minority-carrier capture cross-section with the inverse of the line density of traps. At 300 K, our simulations of carrier occupation and recombination rate match literature electron-beam-induced current (EBIC) data and first-principles calculations of carrier capture, emission, and recombination for all the energy levels associated with dislocations decorated with metal impurities. We implement our model in Sentaurus Device, determining the losses across different device architectures for varying impurity decoration of grain boundaries.

© 2015 The Authors. Published by Elsevier Ltd. This is an open access article under the CC BY-NC-ND license (<http://creativecommons.org/licenses/by-nc-nd/4.0/>).

Peer review by the scientific conference committee of SiliconPV 2015 under responsibility of PSE AG

**Keywords:** Solar cell; photovoltaics; silicon; modeling; dislocation; grain boundary

---

---

\* Corresponding author.

E-mail addresses: [davidbn@alum.mit.edu](mailto:davidbn@alum.mit.edu), [buonassisi@mit.edu](mailto:buonassisi@mit.edu)

## 1. Introduction

The deleterious effects of structural defects (*e.g.*, grain boundaries and dislocations) on solar cell performance are well known [1,2]. Models exist that describe the electrical and recombination activity of these defects [3,4] and show that extended defects have impacts beyond reducing minority carrier lifetime, including locally lowering the junction barrier height, which can reduce the open-circuit voltage ( $V_{oc}$ ) [5]. However, models describing the electrical activity of structural defects typical of commercial mc-Si have not, to our knowledge, been implemented in TCAD device models. Evaluating the potential and materials requirements for highly defective Si (*e.g.*, mc-Si) to achieve very high (>20%) module efficiencies is valuable for planning research and investment to meet PV cost targets [6]. Here, we validate a simple, yet effective, model for structural defects based on material properties, rather than the local recombination rate. We incorporate this model into device simulations using Sentaurus Device to assess performance degradation in different device architectures for varying concentrations of impurities decorating these defects.

## 2. Structural defect model

Kveder *et al.* [3] presented and validated a model for the electrical activity of dislocations based on first principles analysis of carrier capture and recombination statistics for both clean dislocations and those decorated with metal impurities. Stokkan *et al.* [4] have shown that, from an electrical perspective, grain boundaries can be treated as arrays of dislocations. Kveder's model involves transitions between many different energy levels. It was shown previously [7,8] that a simplification to one single energy level near midgap can be done effectively if the grain size is not too small (smaller than usual mc-Si material) and if the doping concentration is not too low (about  $5 \times 10^{15} \text{ cm}^{-3}$  at the usual grain size of mc-Si material). This simplification may also have the advantage that it removes a degree of freedom of the input parameters (the energy distribution of defects) and therefore captures the dynamics of phenomena in a more straightforward way [8]. We find that at 300 K, we can match the enhanced recombination and band bending associated with metals decorating dislocations using a single-energy-level SRH model by transforming the capture cross-sections as follows:

$$\sigma_{\text{majority, single-level}} = \sigma_{\text{majority, actual}} \times a, \quad (1)$$

$$\sigma_{\text{minority, single-level}} = \sigma_{\text{minority, actual}} \times \frac{b}{N_{\text{decoration}}}, \quad (2)$$

where  $N_{\text{decoration}}$  is the line density of metallic impurities, while  $a$  and  $b$  are fitting parameters.

Like Kveder *et al.*, we validate our model by simulating EBIC experiments. We simulate with the TCAD software Sentaurus Device [9] and choose a 2-D domain to match Kveder's simulations and the experiments to which those simulations were fit [10,11]. This domain includes a 10  $\mu\text{m}$ -thick Si wafer with a Schottky contact covering the whole of the top surface. A Schottky barrier height of 0.7 eV is used to match that of aluminium on Si. Our simulated domain is 100  $\mu\text{m}$  wide, although varying the width from 10  $\mu\text{m}$  to 1000  $\mu\text{m}$  does not affect the results. Doping densities of  $5 \times 10^{14} \text{ cm}^{-3}$  and  $1 \times 10^{15} \text{ cm}^{-3}$  are used to match the relevant experiments and Kveder's simulations. The background lifetime of the Si wafer is set to 1  $\mu\text{s}$  based on the reported concentrations of copper and nickel in the wafers used in the experiments and these impurities' known effects on Si lifetime [12]. However, varying the background lifetime from 100 ns to 10 ms does not affect the results. Following the method of Schroder [13], We simulate the excitation due to the 30 keV electron beam used in the experiments as a circular area of diameter 6  $\mu\text{m}$  with a constant generation rate depending on the beam current:

$$G = I_{\text{beam}} (\text{pA}) \times (4.55 \times 10^{20} \text{ pA}^{-1} \text{ cm}^{-3}), \quad (3)$$

We include a dislocation as a  $12.25 \text{ nm}^2$  region (the area of the strain field around the dislocation core) inside the electron-beam excitation volume. Defects are placed at the interface between this region and the surrounding silicon wafer. As inputs to our recombination model, we use the same set of defect parameters extracted by Kveder *et al.* including the line density of the defects as an areal density at the interface by dividing by the perimeter of the interface. We use a 2-D model, since it is significantly faster and fitting our free parameters requires many iterations. However, using a 3-D model with a spherical excitation volume and a rectangular prism rather than a square defining the dislocation changes the current by less than 5% relative. EBIC contrast is calculated using the current from a simulation that includes a dislocation and the current from an identical simulation in which the dislocation/bulk interface contains no defects.

We simultaneously fit EBIC contrast as a function of beam current and  $N_{\text{decoration}}$  as well as band bending around the dislocation. We find  $a = 1.4$  (dimensionless) and  $b = 5.5 \times 10^6 \text{ cm}^{-1}$ . As shown in Fig. 1a, we closely match the experimental EBIC contrast as a function of electron beam current (generation rate).

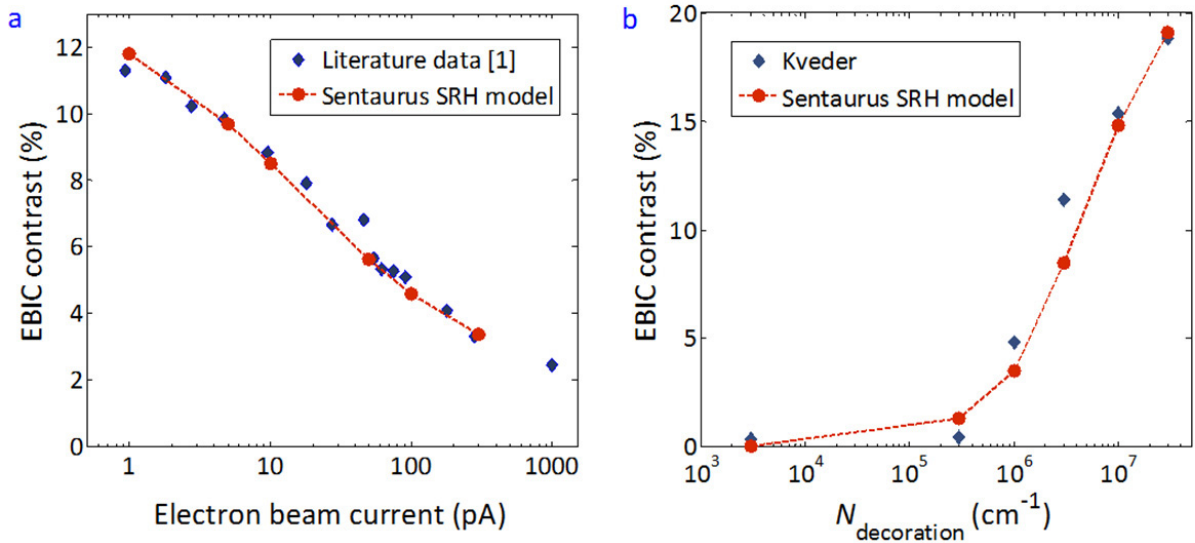


Fig. 1. (a) Simulated and literature experimental data for EBIC contrast vs. electron-beam current; (b) EBIC contrast vs. line density of impurities from Kveder's model and our modified SRH model using Kveder's expression for minority carrier density as a function band bending (from Sentaurus Device simulations).

In Table I, we compare our simulated band bending around the dislocation to values simulated by Kveder *et al.* Kveder assumed a constant minority carrier density at the edge of the depletion region around the charged dislocation. In Sentaurus Device, carrier concentrations are solved self-consistently at every point in the finite element mesh, and there is significant spatial variation within our simulated domain because minority carriers are extracted through the Schottky contact, creating a depletion region near the top surface and a steady-state gradient in minority carrier density through the device thickness. We adjust the generation rate so the peak hole density outside the dislocation space-charge region in our simulations matches Kveder's values.

Table 1. Band bending at dislocation from our model and Kveder's with varying deep trap properties.

$N_{\text{decoration}} (\text{cm}^{-1})$	$\sigma_{\text{min,Kveder}} (\text{cm}^2)$	$\sigma_{\text{min,Sentaurus}} (\text{cm}^2)$	$\sigma_{\text{maj,Kveder}} (\text{cm}^2)$	$\sigma_{\text{maj,Sentaurus}} (\text{cm}^2)$	$\Delta E_{C,\text{Kveder}} (\text{meV})$	$\Delta E_{C,\text{Sentaurus}} (\text{meV})$
$3.0 \times 10^7$	$6.5 \times 10^{-14}$	$1.2 \times 10^{-15}$	$2.0 \times 10^{-15}$	$2.8 \times 10^{-15}$	60	64
$2.4 \times 10^6$	$5.5 \times 10^{-14}$	$1.3 \times 10^{-14}$	$5.0 \times 10^{-14}$	$7.0 \times 10^{-14}$	64	64
$2.2 \times 10^5$	$6.5 \times 10^{-15}$	$1.6 \times 10^{-13}$	$2.0 \times 10^{-15}$	$2.8 \times 10^{-15}$	4	2

Because Kveder *et al.* calculated EBIC contrast from the recombination rate at the dislocation, and we simulate an EBIC experiment, we cannot match their results for EBIC contrast vs. impurity concentration. However, we obtain similar results by taking the band bending from our TCAD simulations, using Kveder's expression for the minority hole density around the dislocation core as a function of band bending, calculating the recombination rate using SRH statistics with our modified capture cross-sections, and converting to EBIC contrast using Kveder's method. These results are presented in Fig. 1b and show good agreement between Kveder's simulations and our own, using Eqs. (1) and (2).

### 3. Device simulation results and discussion

For solar cell simulations, we choose a 3-D domain, which includes a small portion of a solar cell. 3-D simulations have been shown to be necessary to capture the effect that carriers can move toward columnar grain boundaries in two directions, rather than only one as would be the case in a 2-D simulation [7]. The edges of the simulation domain are the center of a contact (front contact in all simulations, both front and rear contacts for local rear contact architectures) on one side and halfway to the next contact on the other side. These are lines of symmetry for carrier transport and can therefore delineate an appropriate unit cell for solar cell simulations. 40  $\mu\text{m}$ -wide front-contact fingers with 1.2 mm spacing (600  $\mu\text{m}$ -wide domain) are used. 200 $\times$ 200  $\mu\text{m}^2$  rear contacts are used for architectures with rear local contacts, corresponding to an area fraction of about 3%.

The grain boundary is implemented as a 2-D interface [7] placed 2 nm from two of the edges of the simulated domain (see Fig. 2). We calculate the areal density of recombination centers at the grain boundary using the method of Stokkan *et al.*, assuming a non-coordinate site lattice grain boundary with a misorientation angle of 2° and varying the line density of recombination sites along the dislocation in the array forming the grain boundary. Square domains are chosen, so that the grains are also square and can be characterized by a single length. For grain sizes smaller than 1.2 mm, the simulated domain and contact dimensions are scaled down proportionally. This proportional scaling gives efficiency,  $V_{OC}$ , short-circuit current density ( $J_{SC}$ ), and fill factor (FF) values for simulations without defects at the grain boundary interface within 5% (relative) for all simulation domain sizes.

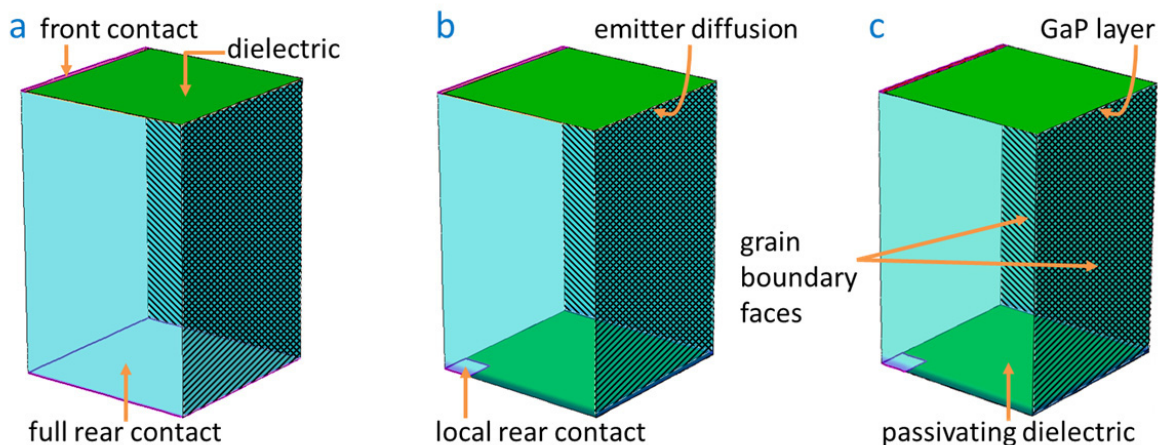


Fig. 2. Schematics of the simulation domains. Grain boundaries are implemented as interface traps on the two right faces of the device (cross-hatched). Note that the interface is actually not the edge of the simulation domain but 2 nm in from the edge. (a) BSF cell with diffused front-side emitter passivated with a dielectric layer and full-area rear contact; (b) PERC cell with identical front-side, but local rear contact and passivating dielectric layer; (c) heterojunction device with GaP emitter, passivating front-side dielectric, and identical rear side to PERC cell.

In the following, we compare the effects of structural defects in three types of devices: industry-standard solar cells with a diffused front junction and full-coverage rear contact with an aluminum back surface field (BSF cell), passivated emitter and rear cell (PERC) with local rear contacts and a passivating dielectric layer between them [14], and a front heterojunction cell with a gallium phosphide (GaP) emitter and the same rear contact configuration as the

PERC cell [15]. For the heterojunction, we use GaP rather than amorphous Si or another emitter material to simulate a perfect heterojunction (ideal band alignment and carrier transport properties) as a best-case scenario for this cell architecture. Parameters like doping density were optimized for each device without the grain boundary included. The doping density in the bulk Si wafer of the heterojunction device is only  $5 \times 10^{14} \text{ cm}^{-3}$ . However, while earlier models were only accurate down to doping densities of about  $5 \times 10^{15} \text{ cm}^{-3}$  [7,8], our ability to accurately simulate EBIC experiments with doping densities down to  $5 \times 10^{14} \text{ cm}^{-3}$  gives us confidence in the accuracy of these simulation results. Schematic diagrams of each of the device architectures are shown in Fig. 2.

The simulated efficiency,  $J_{SC}$ , and  $V_{OC}$  for the BSF and PERC devices with  $100 \mu\text{m}$  grains are shown in Fig. 3, plotted vs. the areal density of recombination centers (metallic impurities) decorating the grain boundary. The PERC and BSF devices behave almost identically as soon as the initially higher performance of the PERC cell is degraded. We do not observe any enhancement of the impact of grain boundaries based on their intersection with the rear contact. The grain boundary in the BSF simulation is under the rear contact because the rear contact covers the whole cell, whereas in the PERC simulation, the grain boundary and the rear contact are on opposite corners of the cell. Additionally, identical results are obtained when the rear contact in the PERC simulation is moved to the same edge as the grain boundary. However, these results do not indicate whether the grain boundary interferes with good contact formation, and we assume for these simulations that it does not.

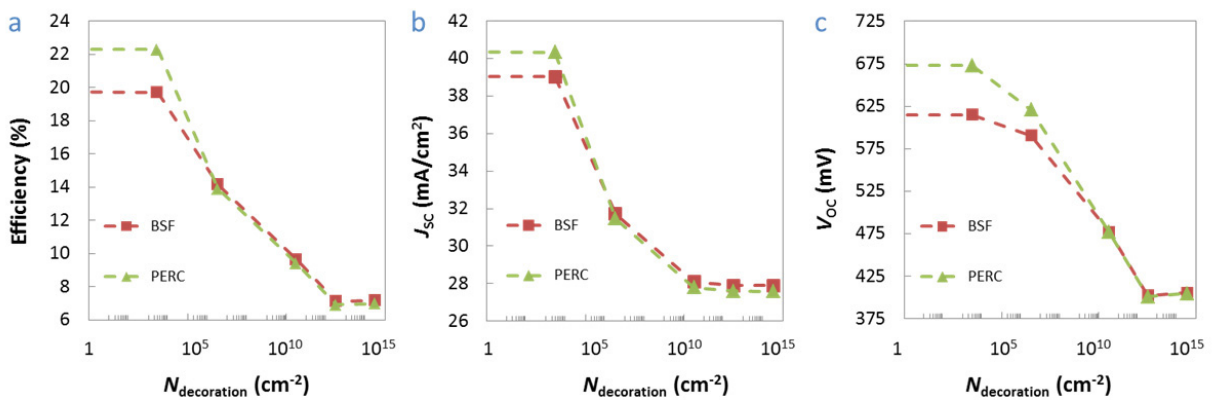


Fig. 3. Simulated device performance metrics plotted vs. areal trap density at the grain boundary for BSF and PERC cells with  $100 \mu\text{m}$  grains. Both devices show nearly identical behavior.

The origin of the similarity in BSF and PERC performance is probed in Fig. 4, which shows the recombination currents in the different regions of the devices as a function of the impurity concentration at the grain boundary. The primary difference between the BSF and PERC cell in the absence of recombination at the grain boundary is the much higher recombination at the rear contact of the BSF cell. As the impurity concentration at the grain boundary increases, the recombination through the grain boundary suppresses this recombination mechanism due to a lower minority carrier density at the high-low junction of the BSF. Greater recombination in the bulk of the device also means fewer minority carriers reach the rear contact, and rear contact recombination actually goes down in the BSF cell. Eventually, at high enough impurity concentrations, grain boundary recombination in the emitter and junction (space-charge) regions becomes significant, though the bulk continues to dominate. Recombination at the grain boundary in all regions is quite similar for both devices.

As can be seen in Fig. 5a, the absence of the grain boundary in the emitter of the heterojunction does not affect the impact of the defect on  $V_{OC}$ , as might be thought from previous work on the effect of extended defects on device performance [5]. Since the grain boundary is recombination-active rather than simply a conductive pathway through the  $p$ - $n$  junction, the effect of bulk recombination (as seen in Fig. 5b) appears to dominate any effects due to a locally lower barrier height near the grain boundary.

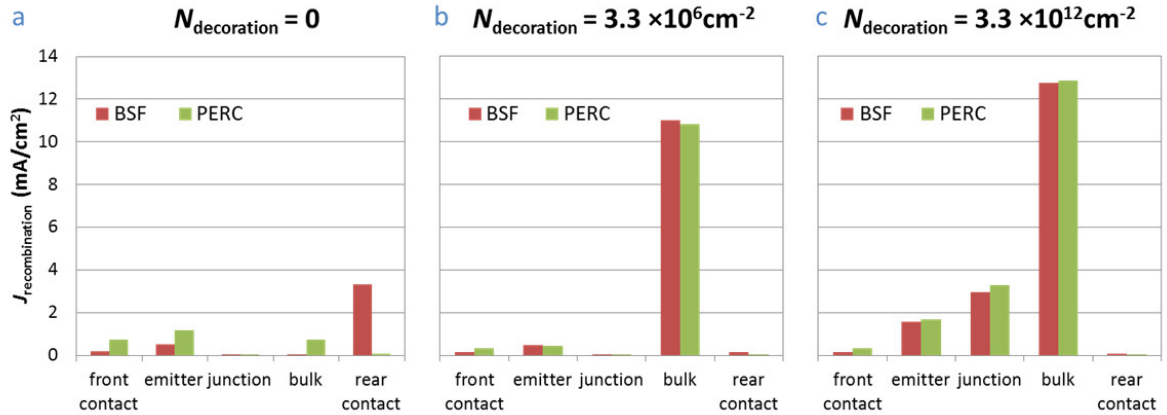


Fig. 4. Recombination current in each region of the BSF and PERC devices at the maximum power point for a fixed grain size of  $100 \mu\text{m}$ . (a) No grain boundary. BSF cell is dominated by rear contact recombination; (b) grain boundary with trap density of  $3.3 \times 10^6 \text{cm}^{-2}$ . Recombination is very similar for both devices and dominated by bulk recombination. Rear contact recombination has decreased for BSF cell, while emitter and front contact recombination have decreased for PERC device due to lower carrier concentrations in these regions; (c) grain boundary with a trap density of  $3.3 \times 10^{12} \text{cm}^{-2}$ . Bulk recombination continues to dominate, but recombination at the grain boundary in the emitter and junction regions becomes significant.

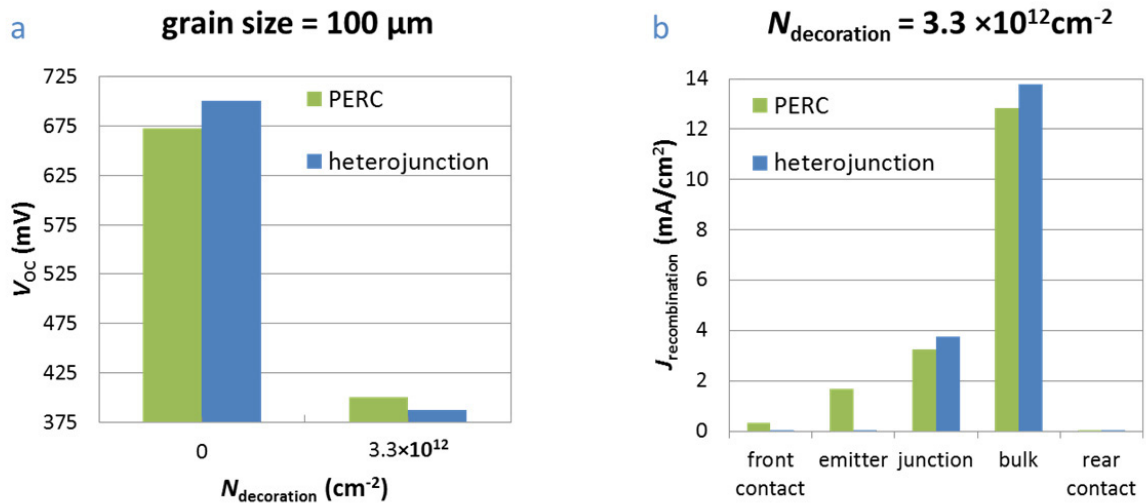


Fig. 5. (a) Heterojunction device voltage does not show increased robustness in the presence of impurity-decorated grain boundaries; (b) recombination current in each region of PERC and heterojunction devices at the maximum power point. Similarity of the two devices voltage responses is attributed to the dominance of bulk recombination.

#### 4. Conclusions

We introduce a model for the electrical impact of structural defects on the device performance of Si solar cells. We validate the recombination rate and band bending of the defects by simulating room temperature EBIC experiments and comparing to literature data and results from a model incorporating the rates of capture and emission from all energy levels associated with these defects. We used this model to simulate BSF, PERC, and front-side heterojunction devices, varying the concentration of impurities decorating grain boundaries. We find that BSF and PERC cells display nearly identical behavior once recombination through the grain boundary overwhelms

recombination at the rear contact. We find no inherent advantage or disadvantage to having a grain boundary sit above the rear contact. We also find that the voltage of both the homojunction and heterojunction devices is determined by bulk recombination rather than local lowering of the  $p$ - $n$  junction barrier height, leading to similar degradation in  $V_{OC}$  from the presence of the grain boundary. We have extended the range of parameters over which we apply a single-defect model (*e.g.*, to lower doping densities). Extension of our model to different grain sizes and other defect types (*i.e.*, dislocations) is straightforward and will enable the establishment of material requirements (grain size, dislocation density, and impurity concentration) for achieving desired device efficiencies. Obtaining direct experimental validation of these solar cell device results will give added confidence in the model.

## Acknowledgements

D. Berney Needleman thanks Dr. Marius Peters (MIT) and Dr. Jasmin Hofstetter for useful conversations and Prof. Filippo Fabbri (U. Bologna) for helpful advice about EBIC. T. Buonassisi acknowledges Ajeet Rohatgi (Georgia Inst. of Technology) for fruitful discussions. This material is based upon work primarily supported by the Engineering Research Center Program of the National Science Foundation and the Office of Energy Efficiency and Renewable Energy of the Department of Energy under NSF Cooperative Agreement No. EEC - 1041895. D. Berney Needleman acknowledges the support of the Department of Defense (DoD) through the National Defense Science & Engineering Graduate Fellowship (NDSEG) program.

## References

- [1] Sopori B. Silicon solar-cell processing for minimizing the influence of impurities and defects. *J Electron Mater* 2002;31:972–80.
- [2] Chen J, Sekiguchi T, Yang D, Yin F, Kido K, Tsurekawa S. Electron-beam-induced current study of grain boundaries in multicrystalline silicon. *J Appl Phys* 2004;96:5490–5.
- [3] Kveder V, Kittler M, Schröter W. Recombination activity of contaminated dislocations in silicon: A model describing electron-beam-induced current contrast behavior. *Phys Rev B* 2001;63.
- [4] Stokkan G, Riepe S, Lohne O, Warta W. Spatially resolved modeling of the combined effect of dislocations and grain boundaries on minority carrier lifetime in multicrystalline silicon. *J Appl Phys* 2007;101:053515.
- [5] Steingrube S, Breitenstein O, Ramspeck K, Glunz S, Schenk A, Altermatt PP. Explanation of commonly observed shunt currents in c-Si solar cells by means of recombination statistics beyond the Shockley-Read-Hall approximation. *J Appl Phys* 2011;110:014515–014515.
- [6] Powell DM, Winkler MT, Choi HJ, Simmons CB, Needleman DB, Buonassisi T. Crystalline silicon photovoltaics: a cost analysis framework for determining technology pathways to reach baseload electricity costs. *Energy Environ Sci* 2012;5:5874–83.
- [7] Altermatt PP, Heiser G. Development of a three-dimensional numerical model of grain boundaries in highly doped polycrystalline silicon and applications to solar cells. *J Appl Phys* 2002;91:4271.
- [8] Altermatt PP, Heiser G. Predicted electronic properties of polycrystalline silicon from three-dimensional device modeling combined with defect-pool model. *J Appl Phys* 2002;92:2561.
- [9] Sentaurus Device User Guide: Version H-2013.03. Synopsys; 2013.
- [10] Kittler M, Ulhaq-Bouillet C, Higgs V. Recombination activity of “clean” and contaminated misfit dislocations in Si (Ge) structures. *Mater Sci Eng B* 1994;24:52–5.
- [11] Kittler M, Seifert W. Two types of electron-beam-induced current behaviour of misfit dislocations in Si (Ge): experimental observations and modelling. *Mater Sci Eng B* 1994;24:78–81.
- [12] Istratov AA, Buonassisi T, Pickett MD, Heuer M, Weber ER. Control of metal impurities in “dirty” multicrystalline silicon for solar cells. *Mater Sci Eng B* 2006;134:282–6.
- [13] Schroder DK. *Semiconductor Material and Device Characterization*. Hoboken, NJ, USA: John Wiley & Sons, Inc.; 2005.
- [14] Altermatt PP. Models for numerical device simulations of crystalline silicon solar cells—a review. *J Comput Electron* 2011;10:314–30.
- [15] Wagner H, Ohrdes T, Dastgheib-Shirazi A, Puthen-Veetil B, König D, Altermatt PP. A numerical simulation study of gallium-phosphide/silicon heterojunction passivated emitter and rear solar cells. *J Appl Phys* 2014;115:044508.